forests

Article

Impacts of Compound Hot–Dry Events on Vegetation Productivity over Northern East Asia

Jing Kang [1], Miao Yu [1,*], Ye Xia [2], Shanlei Sun [1] and Botao Zhou [1]

1 Collaborative Innovation Center on Forecast and Evaluation of Meteorological Disasters/Key Laboratory of Meteorological Disaster, Ministry of Education/Joint International Research Laboratory of Climate and Environment Change (ILCEC), Nanjing University of Information Science & Technology (NUIST), Nanjing 210044, China
2 Key Laboratory of Watershed Geographic Sciences, Nanjing Institute of Geography and Limnology, Chinese Academy of Sciences, Nanjing 210008, China
* Correspondence: yum@nuist.edu.cn; Tel.: +86-137-7650-3727

Abstract: Climate extremes, such as heatwaves and droughts, significantly impact terrestrial ecosystems. This study investigates the influence of compound hot–dry (CHD) events on vegetation productivity in northern East Asia. Four of the most widespread CHD events occurring during the summer from 2003 to 2019 were selected as the focus of this research. We first verified the performance of the Community Land Model version 5 (CLM5) in the region and then conducted factor-controlled experiments using CLM5 to assess the effects of different climate factors on gross primary productivity (GPP) changes during CHD events. Our results show that vegetation productivity exhibits greater sensitivity to CHD events within the transitional climatic zone (TCZ) than in other affected areas. In grassland areas within the TCZ, precipitation deficit is the primary factor leading to the decrease in GPP (explaining 56%–90% of GPP anomalies), while high temperatures serve as a secondary detrimental factor (explaining 13%–32% of GPP anomalies). In high-latitude forests outside the TCZ, high temperature has a more significant impact on suppressing GPP, while the decrease in soil moisture has a synchronously negligible impact on GPP. There are differences in the effects of high solar radiation on grasslands and woodlands during CHD events. It was observed that high radiation benefits trees by increasing the maximum carboxylation rate (V_{cmax}) and maximum electron transport rate (J_{max}), as well as enhancing photosynthesis, but has a negligible impact on grasses. Furthermore, this study highlights the potential for compound events to impact vegetation productivity more than expected from individual events due to confounding nonlinear effects between meteorological factors. More than 10% of the negative anomalies in GPP during two CHD events in 2017 and 2010 were attributed to these nonlinear effects. These research findings are significant for understanding ecosystem responses to climate extremes and their influence on carbon cycling in terrestrial ecosystems. They can also contribute to more precisely evaluating and predicting carbon dynamics in these regions.

Keywords: compound hot–dry events; gross primary productivity; vegetation; northern East Asia

check for updates

Citation: Kang, J.; Yu, M.; Xia, Y.; Sun, S.; Zhou, B. Impacts of Compound Hot–Dry Events on Vegetation Productivity over Northern East Asia. *Forests* **2024**, *15*, 549. https://doi.org/10.3390/f15030549

Academic Editor: Xiuchen Wu

Received: 29 January 2024
Revised: 14 March 2024
Accepted: 15 March 2024
Published: 18 March 2024

1. Introduction

Since the advent of the Industrial Revolution, human-induced greenhouse gas emissions have instigated global climate change, consequently yielding a rise in the frequency and intensity of extreme weather events [1–3]. Owing to their sudden occurrence and inherent unpredictability, these extreme climate phenomena pose a significant peril to human society and the ecological environment [4,5].

Vegetation plays a crucial role in the carbon cycle of terrestrial ecosystems. Gross primary productivity (GPP) is a critical indicator for measuring the products of vegetation photosynthesis [6–8]. However, in recent years, multiple significant extreme events have seriously impacted vegetation GPP. For instance, the extreme heat and drought in Europe in 2003 caused a significant 30% reduction in GPP, almost offsetting four years of ecosystem carbon sequestration [9]; in the summer of 2012, a once-in-a-century drought in the central western United States suppressed crop and grassland growth, with grassland GPP decreasing by 29% [10]. Importantly, studies suggest that concurrent occurrences of heatwaves and droughts (i.e., compound hot–dry (CHD) events) may have greater impacts than individual extremes [11–13]. The prevalence of CHD events is projected to escalate across a majority of regions worldwide throughout the 21st century [14–17]. Considering the severe and devastating consequences associated with CHD events, it becomes imperative to enhance our comprehension and awareness of such events and evaluate their far-reaching impacts on ecosystems.

Although previous studies have assessed the impacts of individual and concurrent extreme events associated with heatwaves and droughts on GPP [13,18,19], there remains a need to understand each process's quantitative contributions comprehensively. Additionally, the underlying physiological processes of vegetation during CHD events have yet to be fully elucidated. Understanding the roles of each climatic factor and accurately quantifying their effects are crucial for further advancements.

One promising approach to unraveling the distinct contributions of individual event drivers involves constraining one (or more) of these drivers within a numerical model [20–22]. By manipulating specific meteorological variables such as precipitation or temperature in a land surface process model and subsequently observing the resulting changes in simulation outcomes, we can gain insights into the eco-hydrological dynamics under different meteorological conditions. This method enables us to explore the impact of specific drivers on the ecosystem and aids in revealing the underlying response mechanisms governing vegetation productivity during CHD events.

Northern East Asia is highly sensitive to climate change and global warming, often experiencing severe impacts from heatwaves and droughts [23–25]. Additionally, this region has abundant vegetation resources and plays a critical role in regional and global carbon balances [26]. Therefore, northern East Asia is ideal for analyzing how vegetation responds to extreme events.

To analyze the impact of CHD events, this study will utilize two key indicators: daily maximum temperature (T_{max}) and the standardized precipitation index (SPI). A hot event will be defined as a period of at least three consecutive days with T_{max} surpassing the 85th percentile threshold. This threshold will be calculated using a 15-day moving window of daily maximum temperatures from 1979 to 2019 [3]. On the other hand, a dry event will be defined as a duration of at least three consecutive days where the SPI < -0.5, following the methodology established by McKee et al. [27]. The SPI is an index obtained by normalizing precipitation for a given time period, assuming that it follows the gamma probability distribution. This study will calculate daily SPI values from daily precipitation data utilizing the "climate_index" package in Python [28], with a time scale of 30 days. A CHD event in each grid cell will be considered when both hot and dry conditions persist for at least three days.

In this study, we assess the impacts of CHD events on GPP over northern East Asia by disentangling the roles of drought and heat using the Community Land Model version 5 (CLM5) with factor-controlled experiments. The objectives of this study are (1) to disentangle and quantify the individual and combined effects of drought and heat on GPP changes during CHD events and (2) to explore the response mechanisms of vegetation productivity to CHD events.

2. Materials and Methods

2.1. Study Area

This study explicitly targets the northern East Asia region, spanning from 105° E to 140° E and 40° N to 60° N (Figure 1). Renowned for its diverse ecosystems encompassing forests, wetlands, and grasslands, this region is crucial in maintaining ecological security. However, given its pronounced warming trends, northern East Asia is becoming increasingly susceptible to heatwaves and droughts [25,29,30], posing a mounting threat to its vegetation. At the same time, due to the interaction of monsoon circulation and westerly belt circulation, a transitional climate zone (TCZ) from humid to arid regions has formed in northern East Asia, which has high ecological vulnerability and climate sensitivity due to this particular climatic condition [31,32].

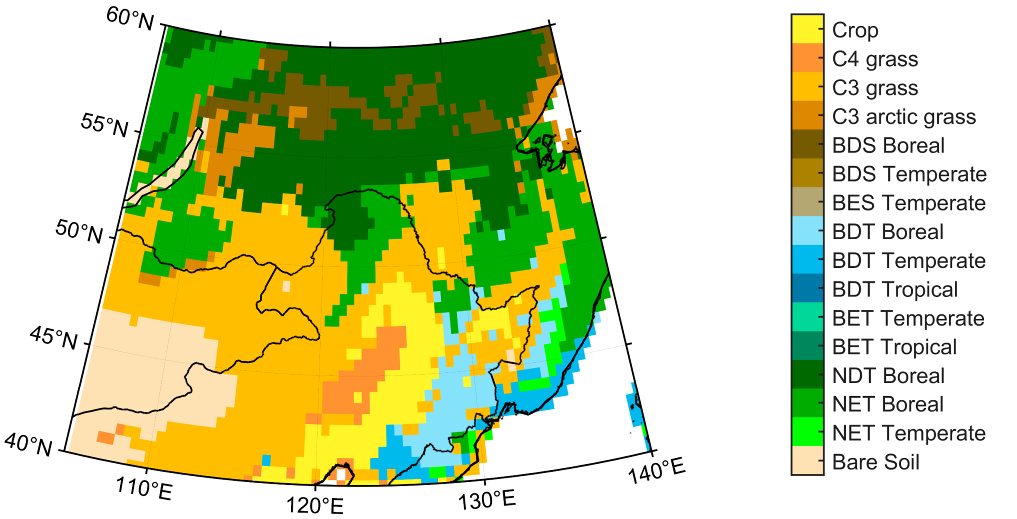

Figure 1. Study area and dominant plant functional type (PFT) distributions. The PFTs are represented by the following abbreviations: B for broadleaf, N for needleleaf, D for deciduous, E for evergreen, S for shrub, and T for tree.

2.2. Model

CLM5, the land surface component of the Community Earth System Model (CESM) version 2.1.3, is used in this study. CLM5 can simulate various terrestrial processes, including the cycling of energy, water, momentum, carbon, nitrogen, and other trace gases [33]. In this study, we perform CLM5 simulations over northeast East Asia in the biogeochemistry (BGC) mode with the "no crop" option. When the BGC mode is active, the vegetation state variables such as leaf area index (LAI), stem area index (SAI), canopy top height, and canopy bottom height are calculated using a prognostic approach [34].

2.3. Experimental Design

The hourly meteorological forcings obtained from the WATCH Forcing Data methodology applied to the ERA5 (WFDE5) dataset from 2003 to 2019 are used to drive CLM5. The WFDE5 dataset covers near-surface atmospheric variables, including precipitation, air temperature, specific humidity, incident shortwave and longwave radiation, surface air pressure, and wind speed at an hourly temporal resolution and 0.5° spatial resolution over the global land surface [35]. To acquire the equilibrium states of the simulated soil and vegetation carbon and nitrogen pools, we performed a 200-year spin-up simulation by cycling the 17 years of WFDE5 forcings in accelerated decomposition mode, followed by another 50 years of spin-up simulation with the accelerated mode turned off. Then, a control run (*Control*) from 2003 to 2019 was restarted from the state at the end of the spin-up simulation.

To explore the combined and individual effects of drought and heat, eight sensitivity experiments were conducted, employing different combinations of atmospheric forcings. The first sensitivity experiment, *SE_Clim*, utilizes climate mean forcings in 2 m temperature, precipitation, incident radiation (including solar and longwave radiation), and 2 m specific humidity during CHD events. The involvement of climatological means in near-surface air pressure and wind basically does not change the simulated results we are concerned about. The difference between the *Control* and *SE_Clim* simulations during the CHD events reveals the combined effect of drought and heat.

The second sensitivity experiment, *SE_PRQ*, focuses on the impact of drought by utilizing forcings with climate means in 2 m temperature. This experiment aims to quantify the influence of precipitation deficit accompanied by atmospheric dryness and enhanced solar radiation while comparing it with *SE_Clim*. The third sensitivity experiment (*SE_RQ*) employs forcings with climate means in 2 m temperature and precipitation to examine the combined effect of incident radiation and air humidity. Additionally, the fourth sensitivity experiment (*SE_TR*) explicitly investigates the combined effect of incident solar radiation and 2 m temperature due to their close relationship.

Subsequent sensitivity experiments, namely *SE_R*, *SE_P*, *SE_T*, and *SE_Q*, are conducted to explore the individual effects of incident radiation, precipitation, 2 m temperature, and 2 m specific humidity, respectively. Each experiment was initiated on January 1 with the same initial conditions and continued for one year. Further details about these experiments can be found in Table 1.

Table 1. Specifics of the experiments.

Experiment No.	Experiment Name	Forcings of the Experiment
	Control	Observed forcings in hourly frequency and 0.5° spatial resolution from 2003 to 2019.
1	*SE_Clim*	Climatological means in 2 m temperature, precipitation, radiation, and 2 m specific humidity during the compound hot–dry (CHD) events.
2	*SE_PRQ*	Similar to *SE_Clim*, but with observed precipitation, radiation, and 2 m specific humidity.
3	*SE_RQ*	Similar to *SE_Clim*, but with observed radiation and 2 m specific humidity.
4	*SE_TR*	Similar to *SE_Clim*, but with observed 2 m temperature and radiation.
5	*SE_R*	Similar to *SE_Clim*, but with observed radiation.
6	*SE_P*	Similar to *SE_Clim*, but with observed precipitation.
7	*SE_T*	Similar to *SE_Clim*, but with observed 2 m temperature.
8	*SE_Q*	Similar to *SE_Clim*, but with observed 2 m specific humidity.

To obtain the climate means of precipitation, the hourly precipitation in every grid cell is derived by multiplying a scaling factor, f_{prcp} [36]. The scaling factor in year *i* is defined as $f_{prcp} = P_{50th}/P_i$. Here, P_i is the event average precipitation during the 30th day before the date when the specified CHD event starts to its end date of the *ith* year. And P_{50th} is the 50th percentile of precipitation of the 41 event averages of precipitation during 1979–2019 [36]. To obtain the climate means of 2 m temperature, the hourly 2 m temperature in every grid cell is calculated by multiplying the scaling factor, f_{tair}, in which $f_{tair} = T_{50th}/T_i$. T_i is the event average of 2 m temperature from the date when the specified CHD event starts to the date when the event ends in the *ith* year. And T_{50th} is the 50th percentile of the average 2 m temperature during 1979–2019. A similar approach to that of deriving the climate means of 2 m temperature was applied for acquiring the climate means in radiative forcings and specific humidity, respectively.

2.4. Observational Data

Observations of GPP, SM, and ET are utilized to analyze the ecological and hydrological characteristics of the CHD events.

The daily GPP data at a spatial resolution of 0.05° were acquired from the Global MODIS and FLUXNET-derived Daily Gross Primary Production (FluxSat) v2.2 dataset [37]. This dataset integrated ground-based station observations to calibrate and validate the MODIS remote sensing data, ensuring precise estimations of GPP with remarkable spatial and temporal resolution.

The daily SM in the depth between the surface and 10 cm depth of soil and ET data were extracted from the Global Land Evaporation Amsterdam Model (GLEAM) v3.7b dataset [38,39]. This dataset utilizes satellite observations to estimate terrestrial evaporation and SM, providing global-scale data with a resolution of 0.25°. These data are of great significance for studying global terrestrial water cycle dynamics, evaluating ET patterns in different ecosystems, and understanding the impacts of climate change [40–42].

The GLEAM and FluxSat datasets are aligned to and averaged at a spatial resolution of 0.5° compared to CLM5.

3. Results

3.1. CHD Events and the Eco-Hydrological Processes

Using the definition methodology mentioned in Section 1, we identified all CHD events in each grid cell in northern East Asia from June to August between 2003 and 2019. Figure 2a depicts the time series of the total area with CHD events, facilitating the identification of periods characterized by regionally extensive and long-lasting CHD events. The most prolonged and regionally extensive CHD events occurred during the summer seasons of 2017 and 2015, with durations of 17 days each. Subsequently, we selected the four most regionally severe CHD events based on the spatial extent for detailed case studies, namely Case2017, Case2015, Case2010, and Case2007. Further information regarding each event's occurrence dates and durations is in Table 2. Figure 2b,c display the spatial distribution of temperature and precipitation anomalies for the four CHD events. All four events show Tmax anomalies above +3 °C and SPI anomalies below −0.5, covering over 34% (1.88×10^6 km^2) of the study area. Case2017 represents the most extensive coverage among these CHD events, with a land area exceeding 61% (3.36×10^6 km^2) affected by drought and heat. The spatial pattern of Case2015 is similar to that of Case2017, albeit with a slightly lower heatwave intensity and higher drought severity in specific areas compared to Case2017. The impact area of Case2010 is more inclined towards the southeast than the first two events, predominantly encompassing forested areas with a small amount of grassland. In the fourth event, Case2007, the affected area is primarily concentrated at the junction of China, Russia, and Mongolia, located in the TCZ, which is also encompassed by Case2017 and Case2015 (45°–55° N, 105°–125° E).

Table 2. Dates and durations of the four selected cases of the regional compound hot–dry events over northern East Asia during summer.

Case ID	Start and End Dates	Duration (Days)
Case2017	22 June 2017–8 July 2017	17
Case2015	4 July 2015–20 July 2015	17
Case2010	22 June 2010–29 June 2010	8
Case2007	23 July 2007–30 July 2007	8

CHD events strongly impact eco-hydrological processes, with our primary focus on the abnormal changes in GPP, ET, and SM. Apart from Case2010, the other three CHD events exhibited noticeable negative anomalies in GPP (Figure 2d). In Case2017 and Case2015, the distribution of GPP anomalies showed remarkable similarity, with 44% and 57% of the vegetation area demonstrating negative GPP anomalies, particularly in the grasslands within the TCZ, where the decline in GPP was most severe. In Case2007, 87% of the vegetation area experienced negative GPP anomalies, and this event witnessed the most significant GPP decrease, with an average reduction of –0.99 gC/m^2/day. Conversely, Case2010 saw a positive impact on GPP due to the combined effects of drought and heatwaves, with 74% of the vegetation area displaying positive GPP anomalies. These findings indicate that different CHD events have varying effects on vegetation productivity, and various types of ecosystems also exhibit distinct responses to these events. During the CHD event, the abnormal performance of ET was closely related to vegetation types. Figure 2e shows that negative ET anomalies were mainly observed in grassland ecosystems.

In contrast, positive ET anomalies were primarily found in forest ecosystems (except for a few boreal evergreen needleleaf trees in the TCZ). Furthermore, the regions with the most significant decline in ET were consistent with those with the largest GPP decrease (see Figure 2d,e). From the spatial distribution of SM anomalies (Figure 2f), it can be observed that the SM in the study area was generally low, except for a small localized area in Case2010.

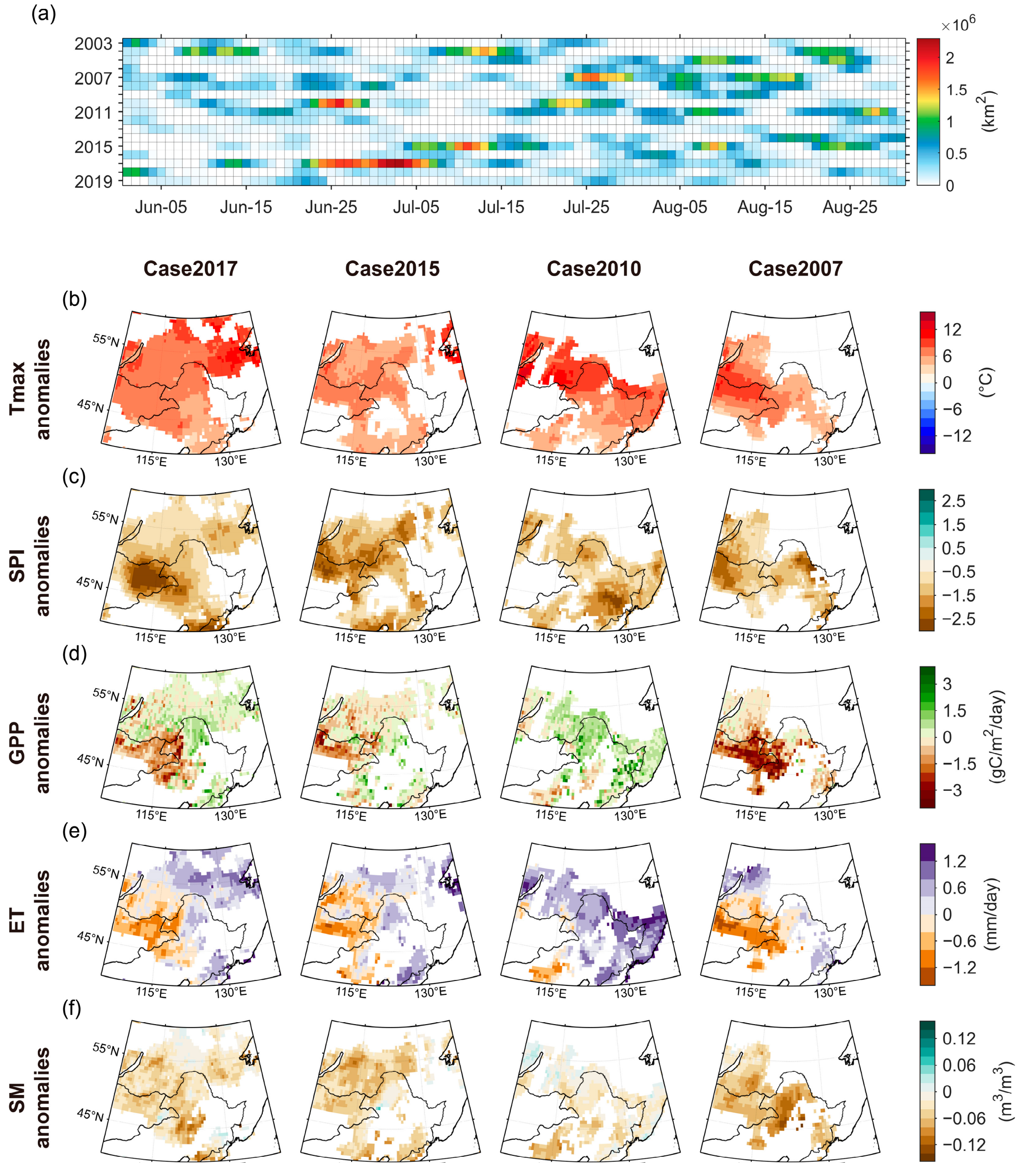

Figure 2. (**a**) The areas with compound hot–dry (CHD) events in summer from 2003 to 2019 across northern East Asia. Anomalies of (**b**) daily maximum temperature (T_{max}), (**c**) standardized precipitation index (SPI), (**d**) gross primary productivity (GPP), (**e**) evapotranspiration (ET), and (**f**) soil moisture (SM) in the top 10 cm of soil for the four selected CHD events compared to the averages during 2003–2019.

3.2. *Performance of CLM5 in Simulating the Eco-Hydrological Processes*

Before exploring the mechanisms of vegetation responses to the CHD events using CLM5, the performance of CLM5 in modeling the eco-hydrological variables, including ET, SM, and GPP, is compared with the observed data.

As shown in Figure 3, the spatial distributions of annual ET, SM, and GPP simulated by CLM5 are similar to the observed distributions. The spatial correlation coefficient between simulated and observed ET is 0.81. CLM5 underestimates ET in most parts of the study area. The Sikhote-Alin Mountain Region bordering the Sea of Japan is underrated, with a bias of more than −200 mm/year (Figure 3g). The ET bias in spring is higher than in other seasons and higher in woodlands than grasslands (Table 3). The spatial correlation of surface SM between simulation and observation is 0.59. The model underestimates SM near Daxinganling and Lake Baikal while overestimating SM in some eastern parts of China (Figure 3h). The spatial correlation coefficient of annual GPP between simulation and observation is 0.68, with a higher value for woodlands than grasslands. GPP is overestimated chiefly in the northern part of 53° N. It is underestimated in some of the southern parts of 53° N, mainly a transition zone of different ecosystems or dominated by deciduous forests (Figure 3i). The model's performance varies in seasons and various types of vegetation. It simulates well the GPP of woodlands in spring and fall, with the spatial correlation coefficients between simulation and observation at 0.71 and 0.87, respectively. Also, it performs well in simulating the summer GPP of grassland, with a spatial correlation coefficient of 0.63 (Table 3).

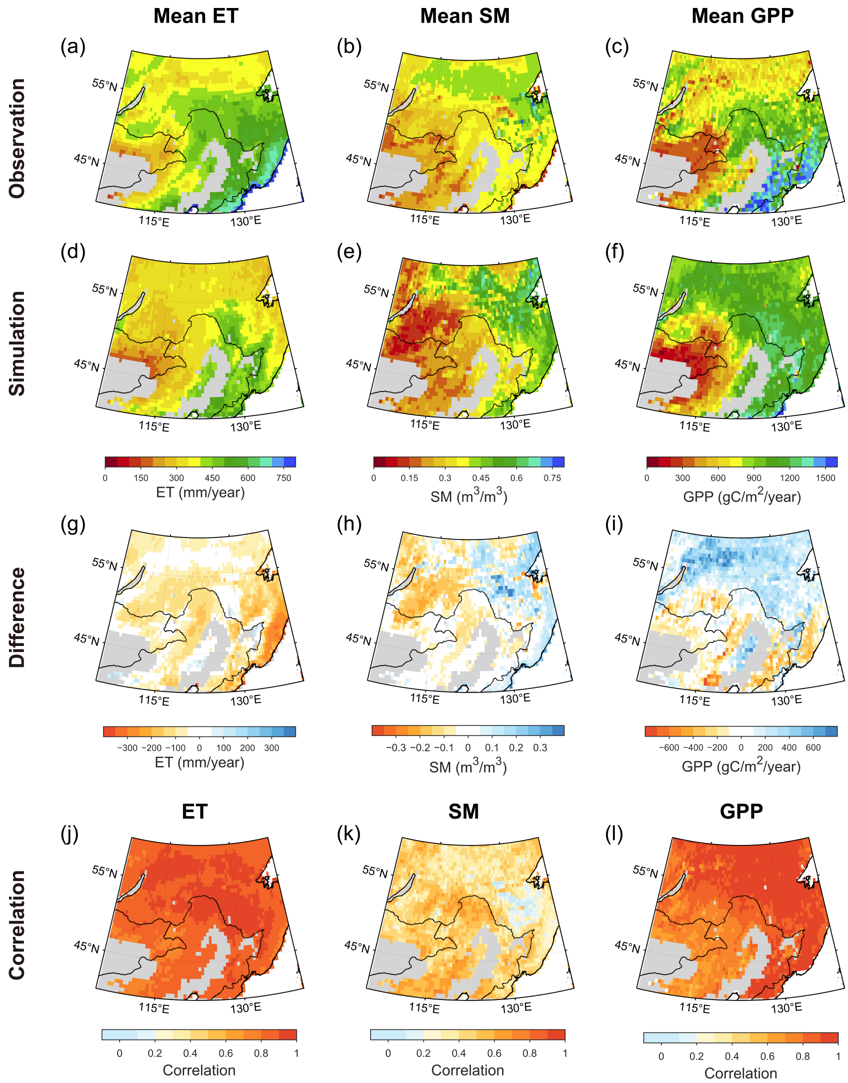

Figure 3. Annual means of the observed evapotranspiration (ET) and soil moisture (SM) in the top 10 cm of soil from GLEAM (**a**,**b**), observed gross primary productivity (GPP) from FluxSat (**c**), simulated ET, SM, and GPP by CLM5 (**d**–**f**) during 2003–2019, and the differences between simulation and observation (**g**–**i**). Correlations (Pearson coefficient) of ET (**j**), SM in the top 10 cm (**k**), and GPP (**l**) between CLM5 and observational datasets on a daily scale from 2003 to 2019. Bare soil and cropland are marked in grey.

Table 3. Performance metrics were utilized to evaluate the CLM5 simulations compared with observed evapotranspiration (ET), soil moisture (SM), and gross primary productivity (GPP) annually and seasonally from 2003 to 2019. The evaluation encompassed bias, relative bias (RB), root mean square error (RMSE), and pattern correlation coefficients (PCCs). Bias and RMSE were measured in units of ET (mm/day), SM (m^3/m^3), and GPP ($gC/m^2/day$), respectively. The seasons were defined as MAM (March–April–May), JJA (June–July–August), SON (September–October–November), and DJF (December–January–February). Furthermore, "grasslands" were classified based on grid cells containing more than 60% grass, while "woodlands" were selected from grid cells comprising over 60% trees and shrubs.

Season	Region	Bias			RB (%)			RMSE			PCC		
		ET	SM	GPP	ET	SM	GPP	ET	SM	GPP	ET	SM	GPP
Annual	All	−0.235	−0.011	0.315	−18.13	−2.62	22.25	0.321	0.113	0.783	0.81	0.59	0.68
	Grasslands	−0.152	−0.033	−0.007	−14.95	−10.46	1.47	0.234	0.073	0.621	0.76	0.59	0.66
	Woodlands	−0.287	−0.002	0.476	−21.17	−0.05	30.70	0.360	0.124	0.812	0.87	0.58	0.75
MAM	All	−0.456	0.040	0.126	−37.96	12.52	12.95	0.520	0.136	0.672	0.80	0.58	0.69
	Grasslands	−0.430	−0.001	−0.155	−44.39	2.42	−28.96	0.483	0.070	0.436	0.69	0.58	0.52
	Woodlands	−0.485	0.060	0.195	−37.51	16.52	20.73	0.545	0.154	0.746	0.84	0.52	0.71
JJA	All	−0.253	−0.094	0.268	−7.85	−24.58	12.53	0.553	0.141	2.475	0.61	0.47	0.46
	Grasslands	−0.010	−0.030	−0.395	0.53	−9.02	−4.06	0.388	0.069	1.804	0.72	0.59	0.63
	Woodlands	−0.389	−0.133	0.748	−12.74	−34.62	21.03	0.617	0.169	2.675	0.65	0.54	0.19
SON	All	−0.128	−0.026	0.913	−14.54	−6.94	113.32	0.212	0.113	1.046	0.89	0.57	0.79
	Grasslands	−0.065	−0.043	0.597	−9.91	−14.42	87.66	0.160	0.076	0.866	0.83	0.61	0.68
	Woodlands	−0.183	−0.018	0.991	−19.97	−4.50	122.98	0.236	0.124	1.045	0.93	0.58	0.87
DJF	All	−0.097	0.036	−0.051	−87.93	8.16	−51.64	0.130	0.182	0.085	0.77	0.54	0.32
	Grasslands	−0.100	−0.056	−0.069	−90.33	−19.49	−82.66	0.115	0.094	0.089	0.86	0.56	0.17
	Woodlands	−0.086	0.084	−0.036	−88.40	21.19	−39.48	0.124	0.212	0.065	0.76	0.54	0.38

Figure 3j–l show the temporal correlation between the simulated and observed datasets on a daily scale. The results show that the model simulates the variation in ET over time very well, with the correlation coefficients ranging from 0.65 to 0.96 and the average value reaching 0.87. CLM5 also performs well in simulating GPP variation, with correlation coefficients ranging from 0.55 to 0.96 and the average value reaching 0.96. Comparatively speaking, the variation in SM is not captured by CLM5, nor are those of ET and GPP, especially in the northeastern part, occupied mainly by woodland.

The CLM5 can capture the responses of ET, SM, and GPP changes well in the four CHD events. Figure 4 shows the changes in these three variables between the *Control* and *SE_Clim* simulations. The spatial patterns and magnitudes are similar to those derived from the observed anomalies in the four events (Figure 2d–f). In particular, the simulated anomalies derived from the *Control* simulation also show similar spatial patterns. However, there are discrepancies between the simulated and observed data regarding the changes in ET and GPP in certain areas southeast of Lake Baikal. The model shows decreases in ET and GPP in these regions, whereas the observations show contrasting trends. This discrepancy suggests a deficiency in the model's ability to accurately simulate eco-hydrological responses in areas dominated by boreal evergreen needleleaf trees. In addition, the model tends to amplify the decrease in GPP in the eastern part of the Mongolian Plateau, which is primarily covered by C3 grasses. Furthermore, the observed increase in GPP in Case2010 is simulated to have an opposite direction of change. Despite these discrepancies, the model successfully captures the decreases in GPP and ET in the eastern part of the Mongolia Plateau, the increase in ET in the northern part of the area, and the overall decrease in SM.

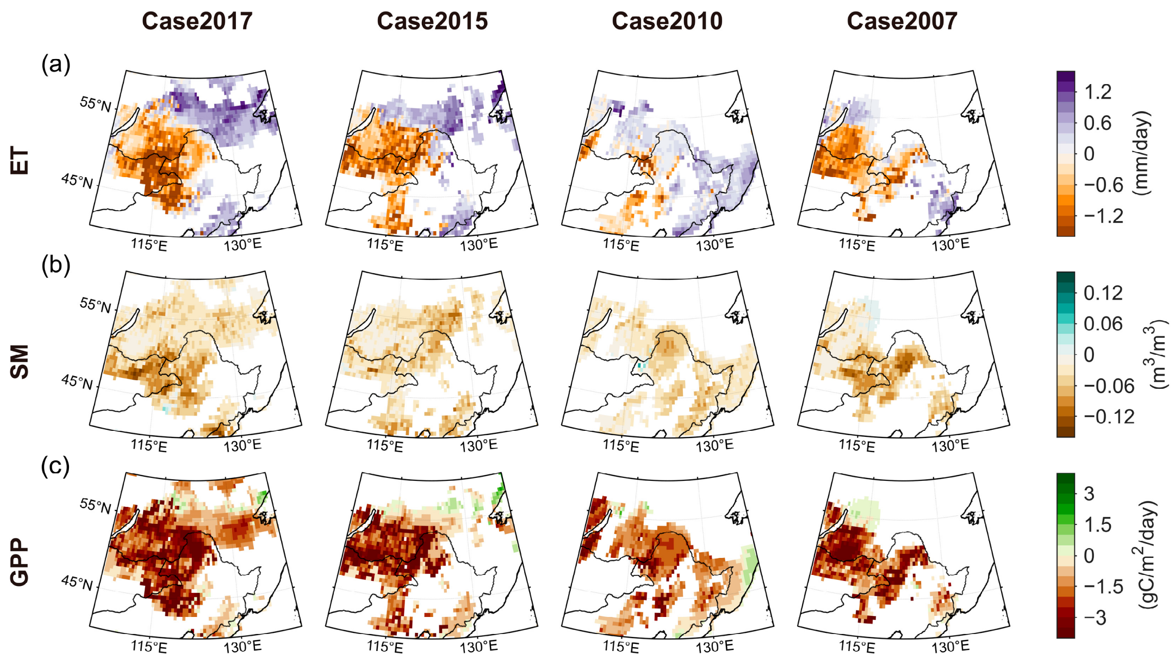

Figure 4. Changes in evapotranspiration (ET) (**a**), soil moisture (SM) (**b**), and gross primary productivity (GPP) (**c**) during the CHD events, calculated by subtracting the results of the *SE_Clim* experiment from those of the *Control* experiment.

The response of ecosystem carbon cycling to the CHD event depends not only on photosynthesis but also on respiration. Figure S1a shows that the changes in autotrophic respiration (AR) simulated by the CLM5 model are generally consistent with the variations in GPP with smaller magnitude. Consequently, there is a pronounced negative anomaly in net primary productivity (NPP), as depicted in Figure S1b. Additionally, the decrease in SM inhibits soil respiration, leading to a substantial reduction in ecosystem respiration (ER), as illustrated in Figure S1c. This partially offsets the simulated carbon loss in some regions, as shown in Figure S1d. Our subsequent analysis focuses on studying different meteorological effects on GPP anomalies when CHD events occur.

3.3. Individual and Compound Effects of Hot and Dry Events

In this part, the simulation results from the factor-controlled experiments by CLM5 are analyzed to disentangle the individual and combined effects of different meteorological factors on terrestrial ecosystems during CHD events. Here, we first show the combination effect of PRQ (precipitation, radiation, and humidity) to investigate the effect of drought with the effects of heat eliminated (panel a in Figure 5 and Figures S2–S6). The combination effect of RQ (radiation and humidity) excludes the effect of precipitation deficit (panel b in Figure 5 and Figures S2–S6). Since the radiation enhancement during the drought events due to cloudless air induces the increase in surface temperature, we show the combination effect of TR (temperature and radiation) and the individual effect of R (radiation) to investigate the impacts of heat and related solar radiation (panels c–d in Figure 5 and Figures S2–S6). The sole effect of T (temperature) on the spatial pattern of GPP changes can be deduced approximately based on the results of the effect of TR minus the effect of R. The results derived from the experiment of *SE_TR* minus *SE_R* show consistent spatial patterns of the GPP decreases compared to the experiment *SE_T* minus *SE_Clim* (Figure S7d), with their magnitude difference being less than 0.35 gC/m^2/day.

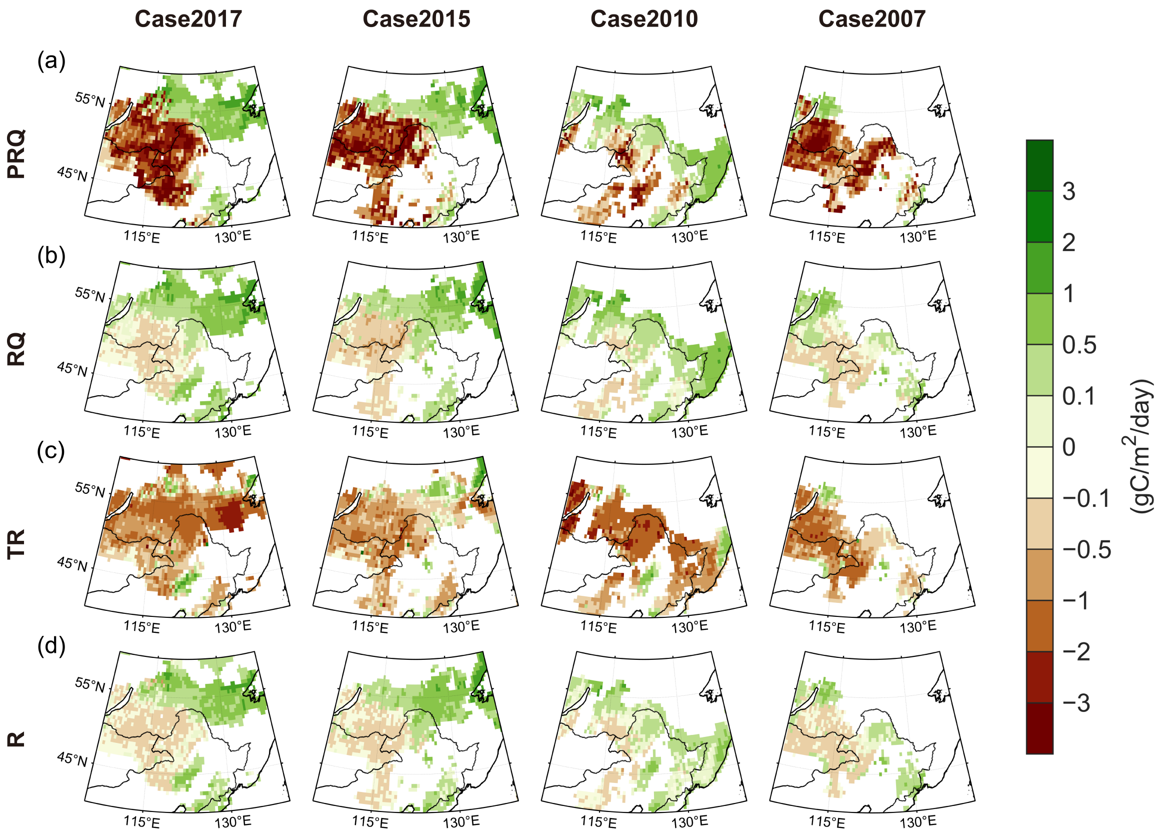

Figure 5. Changes in GPP caused by the combined effects of (**a**) precipitation, incident radiation, and 2 m humidity (PRQ), (**b**) incident radiation and 2 m humidity (RQ), and (**c**) 2 m temperature and incident radiation (TR) and (**d**) the individual effect of incident radiation (R) during the four CHD events. These GPP changes were calculated by subtracting the results of the *SE_Clim* experiment from the results of the *SE_PRQ*, *SE_RQ*, *SE_TR*, and *SE_R* experiments, respectively.

Figure 5 shows the GPP responses in northern East Asia. The results between the four factor-controlled experiments (*SE_PRQ*, *SE_RQ*, *SE_TR*, and *SE_R*) and the *SE_Clim* experiment show that, except for Case2010, drought has a more significant effect on GPP than extremely high temperatures in the TCZ (Figure 5a,c). In the northern part of the region, the effects that exclude heat (PRQ, RQ, and R) consistently show an increase in GPP with similar magnitudes. However, the combined effect of temperature and radiation (TR) has a contrasting trend of GPP change. This suggests that while high solar radiation alone increases GPP, extremely high temperatures caused by high radiation can suppress GPP increase or induce a decrease in GPP. Compared to the combined stress of drought and heatwaves, shown in Figure 4c, the decline in GPP caused by individual droughts or heatwaves alone is smaller than the impact of heat-overlapping drought. Additionally, there is little difference between the combined effect of RQ and the individual effect of R (Figure 5b,d), indicating a slight contribution of near-surface humidity to GPP. This finding is consistent with the results from the experiment using abnormal forcing in 2 m air humidity only (Figure S8d).

Figures S2–S6 show the synchronal changes in soil moisture, VPD, ET, canopy conductance (G_c), and the maximum carboxylation rate (V_{cmax}). These figures provide a visual representation of the data. Figure 6, on the other hand, presents the tabulated form, summarizing these changes concisely and in an organized manner. During drought, the soil moisture decreases prominently and extensively (Figure S2a). Heat also contributes to the decrease in soil moisture by enhancing ET (Figures S2c and S4c). Atmospheric dryness relates closely to abnormal heat (Figure S3c). Abnormal 2 m humidity plays a small but limited role in the increase in VPD, particularly in the TCZ (Figure S3b minus Figure S3d and Figure S8b). Figure S5 shows the changes in G_c to explore the impacts on stomatal resistance. It suggests that the stomatal resistance increases due to both the precipitation deficit and the heat stress, particularly in the TCZ (Figure S5a,c). The enhanced solar radiation contributes to the decrease in G_c to some degree, also probably due to the stomate closure in cases of light saturation (Figure S5d).

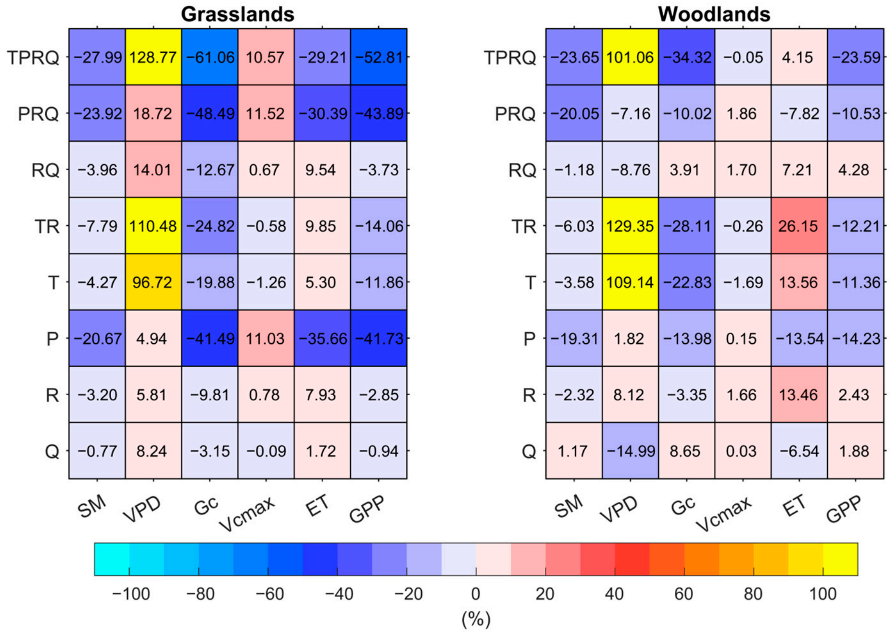

Figure 6. Relative changes in soil moisture (SM), vapor pressure deficit (VPD), stomatal conductance (G_c), maximum stomatal conductance (V_{cmax}), evapotranspiration (ET), and gross primary productivity (GPP) during the four CHD events in grasslands and woodlands. These changes were derived from the *Control* experiment and sensitivity experiments No. 2 to 8, relative to the *SE_Clim*. The combined effects of multiple factors are denoted as TPRQ (temperature, precipitation, radiation, and humidity), PRQ (precipitation, radiation, and humidity), RQ (radiation and humidity), and TR (temperature and radiation), while individual effects are represented by T (temperature), P (precipitation), R (radiation), and Q (humidity). "Grasslands" and "woodlands" refer to areas with vegetation cover consisting of over 60% grass and over 60% trees and shrubs, respectively.

Overall, we can find that the terrestrial GPP over this area is impacted firstly by precipitation deficit and secondly by extreme heat during these four CHD events. However, the TCZ covered mainly by grass shows different responses in GPP to solar radiation changes compared to that in the high-latitude forest-dominated area.

Firstly, the reduction in sub-surface SM during droughts has a limited effect on forest ecosystems (Figures 5a and S2a). This is probably because tree root systems penetrate deeper than grass into the soil in search of water. In addition, the increase in incoming radiation during drought due to cloudless conditions promotes the photosynthesis of trees. However, the extremely high temperatures during these four CHD events may surpass the maximum carboxylation temperature, reducing enzyme activities and photosynthesis (Figure S6c).

Secondly, the VPD increases more due to extreme heat in grasslands than in forests (Figure S3c). The atmospheric dryness is compensated to some degree by ET, and this effect is more prominent in woodlands than in grasslands (Figure S4). Larger VPD increases further induce larger G_c reduction (Figure S5c), reducing GPP more in grasses than in forests.

Thirdly, G_c is sensitive to decreases in SM in the TCZ (Figure S5a), and plants control water evaporation by regulating stomatal closure to reduce water loss (Figure S3a). The stomatal closure limits gas exchange, resulting in the inability of plants to access CO_2, which further inhibits photosynthesis and thus reduces GPP. In addition, physiological changes in vegetation under severe drought conditions reduce leaf area (figure omitted), resulting in a severe disruption of vegetation function and structure. Drought conditions are often accompanied by high incoming radiation. High-intensity radiation could increase the leaf temperature of grassland ecosystems, affecting plant physiological activity by reducing G_c (Figure S5b).

To quantitatively estimate the role of each variable in the GPP changes during the CHD events, the averaged changes in GPP are calculated based on the *Control* experiment and factor-controlled experiments minus the *SE_Clim* experiment for forests and grasslands, respectively (Figure 7).

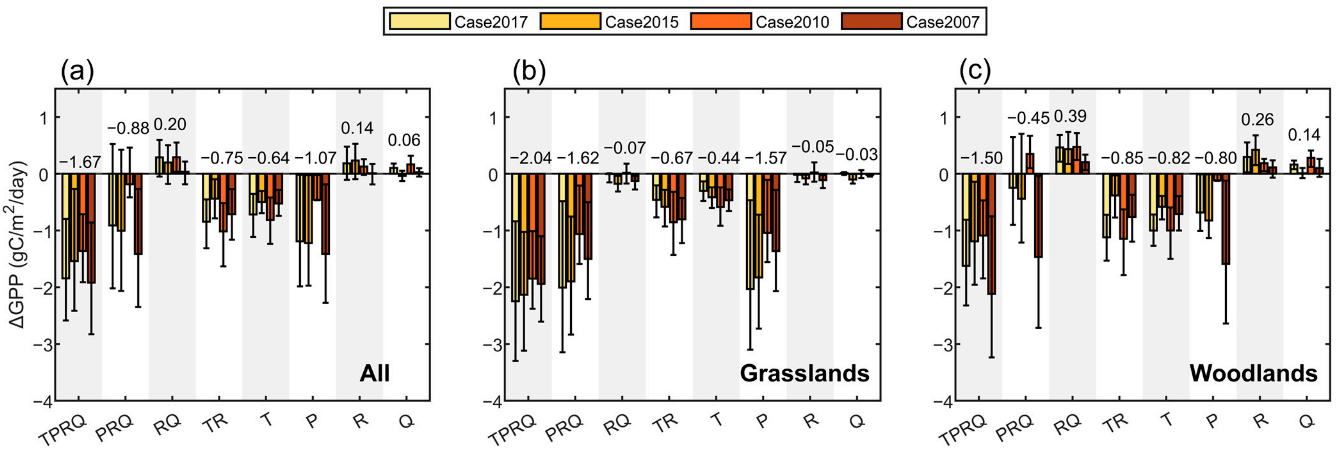

Figure 7. Regionally and temporally averaged changes in gross primary productivity (GPP) derived from the results from the *Control* experiment and sensitivity experiments No. 2 to 8 relative to the *SE_Clim* in (**a**) all affected areas, (**b**) grasslands, and (**c**) woodlands during the four CHD events. The boxes show the average GPP changes across different scenarios; the whiskers indicate the 25th to 75th percentiles of change. In each case (**a**–**c**), the average value of the four CHD events is written above the respective experiment. The combined effects of multiple factors are denoted as TPRQ (temperature, precipitation, radiation, and humidity), PRQ (precipitation, radiation, and humidity), RQ (radiation and humidity), and TR (temperature and radiation), while individual effects are represented by T (temperature), P (precipitation), R (radiation), and Q (humidity). "Grasslands" and "woodlands" refer to grid cells with over 60% grass and over 60% trees and shrubs, respectively.

The impact of the CHD events resulted in an average decrease of $-1.67 \mathrm{gC/m^2/day}$ in GPP. The decline in GPP was higher in grasslands (-2.04 gC/m^2/day) than in forests (-1.50 gC/m^2/day). In grassland ecosystems, drought was identified as the primary factor contributing to the reduction in GPP, with the PRQ effect causing an average decrease of 1.62 gC/m^2/day. The secondary factor was extremely high temperatures, with the TR effect leading to a reduction of 0.67 gC/m^2/day in grassland GPP. The influences of R and Q (atmosphere humidity) can be considered negligible. In forest ecosystems, the changes in GPP during the CHD event were determined by multiple factors. High temperatures had a robust limiting effect on tree GPP, resulting in an average decrease of 0.82 gCm^2/day. Compared to grasslands, R and Q were more important climate factors for forests. High radiation caused an average increase of 0.26 gC/m^2/day in GPP, and local atmosphere humidity led to a rise of 0.14 gC/m^2/day in GPP.

Figure 8 shows the contributions of different variables to the GPP changes. The difference between the *Control* experiment and the *SE_Clim* experiment represents the total effect (TPRQ) of CHD events, and the proportions of the effects of P (precipitation), T, R, and Q on the total effect are calculated. The residual terms are treated as the confounding or nonlinear effects between variables. In grassland ecosystems, insufficient precipitation emerges as the primary driver of the GPP decline, accounting for 56% to 90% of GPP anomalies observed in different events. Conversely, high temperatures contribute modestly, explaining 13% to 32% of GPP anomalies, while radiation and humidity effects remain generally negligible. High-latitude forests demonstrate that the inhibitory effect of extremely high temperatures on tree GPP can account for over 33% of GPP anomalies across various events. In contrast, water limitation resulting from meteorological drought may not pose a severe threat to trees, contingent upon drought intensity and species resilience, with local atmospheric humidity conditions exerting some influence. The effects of residual terms cannot be neglected in CHD events. In Case2017 and Case2010, the residual terms significantly negatively contribute to GPP changes, explaining 12% and 28% of GPP anomalies, respectively. Compared to grassland ecosystems, the impact of residual terms on GPP changes is greater in forest ecosystems.

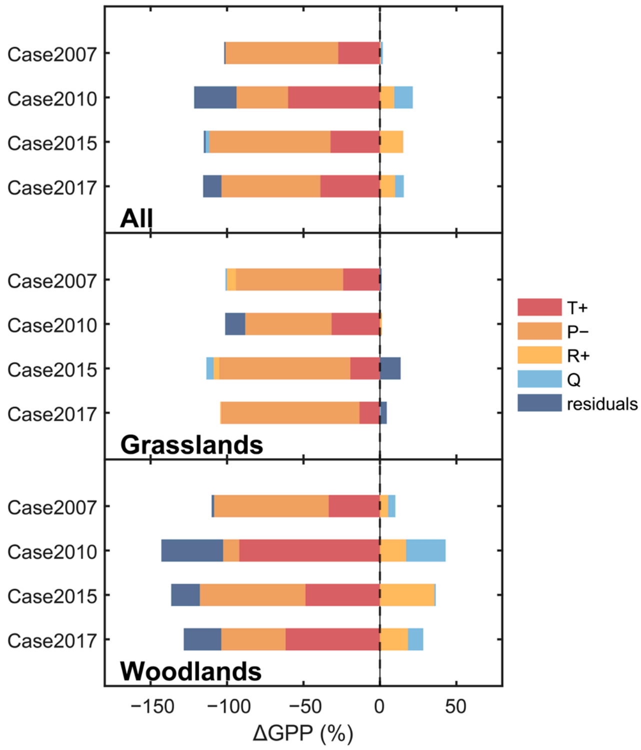

Figure 8. Contributions of various climatic factors to GPP changes for the four CHD events derived from the comparison between sensitivity experiments with one abnormal variable and with all abnormal variables. Marks of minus and plus represent the increase and decrease in variables. "Grasslands" and "woodlands" refer to grid cells with over 60% grass and over 60% trees and shrubs, respectively.

4. Discussion

4.1. The Roles of Drought and Heat in GPP Changes during CHD Events

Precipitation deficits have decreased GPP, with grasslands being significantly more sensitive to such events than forests. This finding is consistent with previous research results [43–45]. In contrast to grasslands, trees typically have deeper root systems, allowing them to access deeper soil moisture levels, thus enabling them to sustain their physiological activities during the early stages of drought [44,46–48]. On the other hand, grassland plants have shallower root systems that are primarily concentrated in the upper soil layers, limiting their ability to access water during dry conditions [45]. Due to water limitations, this may lead to stomatal closure, thereby reducing photosynthesis and transpiration. Plant leaves may be damaged in severe and prolonged drought [49], directly leading to a significant decrease in GPP.

Under non-drought conditions, extremely high temperatures also inhibit GPP, serving as the second-largest factor influencing grassland GPP changes and a key driver behind the simulated decline in high-latitude forest GPP. While studies by von Buttlar et al. [13] suggest that extreme temperatures without accompanying drought have minimal to no negative impact on GPP in most cases, other research indicates that heatwaves can indirectly cause water stress, leading to GPP reductions [50,51]. Moreover, prolonged and intense heatwave events may significantly affect GPP negatively [13], and the seasonality of heatwaves also plays a crucial role in their impact [52]. Extreme high temperatures can restrict GPP in two ways. On the one hand, they may directly impact enzyme activity, leading to a decrease in the activity of the key enzyme Rubisco involved in photosynthesis [53], resulting in a decrease in V_{cmax}/J_{max}, thereby causing a reduction in GPP. On the other hand, extremely high temperatures can also cause abnormally high VPD. If this situation persists for a long time, even with soil moisture present, plants may be forced to reduce G_c to prevent embolisms in the xylem [54].

Further analysis in this study reveals that excluding the influence of high temperatures, the combined effects of other factors appear to promote GPP in high-latitude forests. However, only when considering the impact of high temperatures do we observe the negative GPP response that is consistent with actual observations. While the models may overestimate the adverse effects of extremely high temperatures, this analysis, to some extent, highlights the significant threat posed by extremely high temperatures to GPP in high-latitude forests during CHD events.

There is a close connection between heatwaves and drought [55]. Heatwaves typically lead to abnormally high temperatures, exacerbating soil moisture evaporation and vegetation transpiration rates, and intensifying drought severity and scope. The unusually high VPD triggered by heatwaves accelerates soil moisture loss, leading to soil dryness and worsening the impact of drought. On the other hand, drought itself can also cause temperature increases as the lack of vegetation transpiration reduces atmospheric moisture content, making surface temperatures more liable to rise. This positive feedback loop exacerbates both heatwaves and drought, forming a vicious cycle. Extreme temperatures and severe drought can both damage plants. Still, in cases where they are combined, plants need to balance strategies of closing stomata to prevent dehydration and keeping stomata open to enhance evaporative cooling [56]. This trade-off may lead plants to sacrifice some carbon absorption and photosynthetic efficiency in extreme conditions for improved survival and adaptability.

4.2. Uncertainties and Limitations of This Study

The identification of CHD events poses a significant challenge due to the varying criteria for drought and heat across diverse regions and ecosystems. In this study, a 30-day SPI was used as a drought indicator, with a threshold of SPI < -0.5 defining dry events. However, it is crucial to recognize that the SPI, being primarily a meteorological drought index based on precipitation, may not fully capture drought events that exert physiological impacts on vegetation for certain ecosystems. For instance, in northern ecosystems, even when the SPI is below -0.5, the soil moisture content may still ensure normal physiological activity of vegetation, thus not significantly influencing GPP. Consequently, the definition of dry events used in this study may limit the assessment of drought impacts on GPP. Multiple factors should be considered to enhance the accuracy of evaluating such impacts, including regional and ecosystem characteristics, and appropriate indicators and thresholds should be selected.

Furthermore, the outcomes of our study may be influenced by the choice of model employed. In particular, CLM5 can barely reproduce the observed anomalous GPP in the southern Yablonov Mountains and the Daxinganling region, which are mostly covered by coniferous forests. Thus, the results discussing forested areas in Section 3 need more certainty. Also, we did not consider feedback from land to the atmosphere. For example, the large decrease in soil moisture did not affect VPD (Figures S2a and S3a), but real-world processes are complex. Land–atmosphere feedback from dry soil is vital for the occurrence of heatwaves and atmospheric droughts [57,58], which, if not considered, may leave some uncertainty in our results.

It is important to emphasize that our study focuses exclusively on natural vegetation and needs to comprehensively examine the impact of extreme climate events on crop growth. Nonetheless, the vital role of crops in ensuring global food security and sustainable agriculture cannot be overstated. Future research endeavors will prioritize exploring how crops respond and adapt to extreme climate events.

5. Conclusions

This study employed factor-controlled experiments using the CLM5 model to dissect the impacts of CHD events on vegetation productivity and to assess the roles of various meteorological factors. Despite some biases compared to observational data, CLM5 could effectively simulate the eco-hydrological responses during CHD events. Within the TCZ, GPP exhibited a particularly sensitive response to CHD events, while outside the TCZ, this response was relatively weak. In ecosystems primarily composed of grasslands within the TCZ, insufficient precipitation was identified as the primary cause of GPP decline, with high temperatures playing a secondary negative role. Conversely, in high-latitude forested areas outside the TCZ, the suppressive effect of high temperatures on GPP was more pronounced than that of drought. Under CHD conditions, confounding or nonlinear effects among meteorological factors were primarily identified in forest ecosystems, potentially exacerbating the negative anomalies in GPP. By quantifying the impacts of drought and heat on GPP changes during CHD events, this study identified dominant factors influencing GPP across ecosystems and analyzed associated biophysical processes. It offers valuable insights into vegetation productivity responses to hot and dry conditions, emphasizing the importance of understanding interactions between drought, high temperatures, and other meteorological factors in different ecosystems across northern East Asia.

Supplementary Materials: The following supporting information can be downloaded at https://www.mdpi.com/article/10.3390/f15030549/s1: Figure S1: Changes in autotrophic respiration (AR) (a), net primary productivity (NPP) (b), ecosystem respiration (ER) (c), and net ecosystem productivity (NEP) (d) during the four compound hot–dry (CHD) events. Figure S2: Changes in soil moisture (SM) caused by the combined effect of (a) precipitation, incident radiation, and 2 m humidity (PRQ), (b) incident radiation and 2 m humidity (RQ), and (c) 2 m temperature and incident radiation (TR), and (d) the individual effect of incident radiation (R) during the four CHD events. Figure S3: Same as Figure S2, but for vapor pressure deficit (VPD). Figure S4: Same as Figure S2, but for evapotranspiration (ET). Figure S5: Same as Figure S2, but for canopy conductance (G_c). Figure S6: Same as Figure S2, but for maximum carboxylation rate (V_{cmax}). Figure S7: The eco-hydrological response of the 2 m temperature's (T) effect, calculated as *SE_Q* minus *SE_Clim*. Figure S8: The eco-hydrological response of 2 m specific humidity's (Q) effect, calculated as *SE_Q* minus *SE_Clim*.

Author Contributions: Conceptualization, M.Y.; methodology, M.Y., S.S. and J.K.; software, J.K. and Y.X.; validation, J.K.; formal analysis, J.K. and M.Y.; investigation, J.K.; resources, M.Y. and B.Z.; data curation, J.K.; writing—original draft preparation, J.K.; writing—review and editing, M.Y.; visualization, J.K.; supervision, M.Y. and S.S.; project administration, M.Y. and B.Z.; funding acquisition, B.Z. and M.Y. All authors have read and agreed to the published version of the manuscript.

Funding: This research was funded by the National Natural Science Foundation of China (grant numbers 41991285 and 42075115).

Data Availability Statement: The FluxSat GPP data were obtained from https://avdc.gsfc.nasa.gov/pub/tmp/FluxSat_GPP/0.05x0.05 (accessed on 15 July 2023). The daily observational data for SM and ET were sourced from the GLEAM dataset, which can be found on a server and accessed through SFTP. The passwords to access the data can be obtained from https://www.gleam.eu (accessed on 27 August 2023). The meteorological data used in this work were obtained from the WFDE5 dataset (https://cds.climate.copernicus.eu/cdsapp#!/dataset/10.24381/cds.20d54e34?tab=form, accessed on 15 July 2023).

Acknowledgments: We would like to thank Guiling Wang at the University of Connecticut for her constructive comments on constructing the numerical simulations. Also, we acknowledge the High Performance Computing Center of Nanjing University of Information Science & Technology for their support of this work.

Conflicts of Interest: The authors declare no conflicts of interest.

References

1. Masson-Delmotte, V.; Zhai, P.; Pirani, A.; Connors, S.L.; Péan, C.; Berger, S.; Caud, N.; Chen, Y.; Goldfarb, L.; Gomis, M.I. (Eds.) *IPCC, 2021: Climate Change 2021: The Physical Science Basis. Contribution of Working Group I to the Sixth Assessment Report of the Intergovernmental Panel on Climate Change*; Cambridge University Press: Cambridge, UK; New York, NY, USA, 2021; *in press*. [CrossRef]
2. Perkins-Kirkpatrick, S.E.; Lewis, S.C. Increasing Trends in Regional Heatwaves. *Nat. Commun.* **2020**, *11*, 3357. [CrossRef]
3. Fischer, E.M.; Sippel, S.; Knutti, R. Increasing Probability of Record-Shattering Climate Extremes. *Nat. Clim. Chang.* **2021**, *11*, 689–695. [CrossRef]
4. Frank, D.; Reichstein, M.; Bahn, M.; Thonicke, K.; Frank, D.; Mahecha, M.D.; Smith, P.; van der Velde, M.; Vicca, S.; Babst, F.; et al. Effects of Climate Extremes on the Terrestrial Carbon Cycle: Concepts, Processes and Potential Future Impacts. *Glob. Chang. Biol.* **2015**, *21*, 2861–2880. [CrossRef]
5. Tschumi, E.; Zscheischler, J. Countrywide Climate Features during Recorded Climate-Related Disasters. *Clim. Chang.* **2020**, *158*, 593–609. [CrossRef]
6. Zhang, Y.; Ye, A. Would the Obtainable Gross Primary Productivity (GPP) Products Stand up? A Critical Assessment of 45 Global GPP Products. *Sci. Total Environ.* **2021**, *783*, 146965. [CrossRef]
7. Liao, Z.; Zhou, B.; Zhu, J.; Jia, H.; Fei, X. A Critical Review of Methods, Principles and Progress for Estimating the Gross Primary Productivity of Terrestrial Ecosystems. *Front. Environ. Sci.* **2023**, *11*, 1093095. [CrossRef]
8. Das, R.; Chaturvedi, R.K.; Roy, A.; Karmakar, S.; Ghosh, S. Warming Inhibits Increases in Vegetation Net Primary Productivity despite Greening in India. *Sci. Rep.* **2023**, *13*, 21309. [CrossRef]
9. Ciais, P.; Reichstein, M.; Viovy, N.; Granier, A.; Ogée, J.; Allard, V.; Aubinet, M.; Buchmann, N.; Bernhofer, C.; Carrara, A.; et al. Europe-Wide Reduction in Primary Productivity Caused by the Heat and Drought in 2003. *Nature* **2005**, *437*, 529–533. [CrossRef]
10. Jin, C.; Luo, X.; Xiao, X.; Dong, J.; Li, X.; Yang, J.; Zhao, D. The 2012 Flash Drought Threatened US Midwest Agroecosystems. *Chin. Geogr. Sci.* **2019**, *29*, 768–783. [CrossRef]
11. Hao, Y.; Hao, Z.; Fu, Y.; Feng, S.; Zhang, X.; Wu, X.; Hao, F. Probabilistic Assessments of the Impacts of Compound Dry and Hot Events on Global Vegetation during Growing Seasons. *Environ. Res. Lett.* **2021**, *16*, 074055. [CrossRef]
12. Zscheischler, J.; Seneviratne, S.I. Dependence of Drivers Affects Risks Associated with Compound Events. *Sci. Adv.* **2017**, *3*, e1700263. [CrossRef]
13. von Buttlar, J.; Zscheischler, J.; Rammig, A.; Sippel, S.; Reichstein, M.; Knohl, A.; Jung, M.; Menzer, O.; Arain, M.A.; Buchmann, N.; et al. Impacts of Droughts and Extreme-Temperature Events on Gross Primary Production and Ecosystem Respiration: A Systematic Assessment across Ecosystems and Climate Zones. *Biogeosciences* **2018**, *15*, 1293–1318. [CrossRef]
14. Tabari, H.; Willems, P. Global Risk Assessment of Compound Hot-Dry Events in the Context of Future Climate Change and Socioeconomic Factors. *NPJ Clim. Atmos. Sci.* **2023**, *6*, 74. [CrossRef]
15. Zhang, Q.; She, D.; Zhang, L.; Wang, G.; Chen, J.; Hao, Z. High Sensitivity of Compound Drought and Heatwave Events to Global Warming in the Future. *Earths Future* **2022**, *10*, e2022EF002833. [CrossRef]
16. De Luca, P.; Donat, M.G. Projected Changes in Hot, Dry, and Compound Hot-Dry Extremes Over Global Land Regions. *Geophys. Res. Lett.* **2023**, *50*, e2022GL102493. [CrossRef]
17. Xu, C.; McDowell, N.G.; Fisher, R.A.; Wei, L.; Sevanto, S.; Christoffersen, B.O.; Weng, E.; Middleton, R.S. Increasing Impacts of Extreme Droughts on Vegetation Productivity under Climate Change. *Nat. Clim. Chang.* **2019**, *9*, 948–953. [CrossRef]
18. Wu, X.; Jiang, D. Probabilistic Impacts of Compound Dry and Hot Events on Global Gross Primary Production. *Environ. Res. Lett.* **2022**, *17*, 034049. [CrossRef]
19. Zhou, S.; Zhang, Y.; Park Williams, A.; Gentine, P. Projected Increases in Intensity, Frequency, and Terrestrial Carbon Costs of Compound Drought and Aridity Events. *Sci. Adv.* **2019**, *5*, eaau5740. [CrossRef]
20. Tschumi, E.; Lienert, S.; van der Wiel, K.; Joos, F.; Zscheischler, J. The Effects of Varying Drought-Heat Signatures on Terrestrial Carbon Dynamics and Vegetation Composition. *Biogeosciences* **2022**, *19*, 1979–1993. [CrossRef]
21. Wehrli, K.; Guillod, B.P.; Hauser, M.; Leclair, M.; Seneviratne, S.I. Identifying Key Driving Processes of Major Recent Heat Waves. *J. Geophys. Res. Atmos.* **2019**, *124*, 11746–11765. [CrossRef]
22. Sun, S.; Liu, Y.; Chen, H.; Ju, W.; Xu, C.-Y.; Liu, Y.; Zhou, B.; Zhou, Y.; Zhou, Y.; Yu, M. Causes for the Increases in Both Evapotranspiration and Water Yield over Vegetated Mainland China during the Last Two Decades. *Agric. For. Meteorol.* **2022**, *324*, 109118. [CrossRef]
23. Sun, C.; Zhu, L.; Liu, Y.; Hao, Z.; Zhang, J. Changes in the Drought Condition over Northern East Asia and the Connections with Extreme Temperature and Precipitation Indices. *Glob. Planet. Chang.* **2021**, *207*, 103645. [CrossRef]

24. Zhang, P.; Jeong, J.-H.; Yoon, J.-H.; Kim, H.; Wang, S.-Y.S.; Linderholm, H.W.; Fang, K.; Wu, X.; Chen, D. Abrupt Shift to Hotter and Drier Climate over Inner East Asia beyond the Tipping Point. *Science* **2020**, *370*, 1095–1099. [CrossRef]
25. Seo, Y.-W.; Ha, K.-J. Changes in Land-Atmosphere Coupling Increase Compound Drought and Heatwaves over Northern East Asia. *NPJ Clim. Atmos. Sci.* **2022**, *5*, 100. [CrossRef]
26. Hu, L.; Fan, W.; Yuan, W.; Ren, H.; Cui, Y. Spatiotemporal Variation of Vegetation Productivity and Its Feedback to Climate Change in Northeast China over the Last 30 Years. *Remote Sens.* **2021**, *13*, 951. [CrossRef]
27. McKee, T.B.; Doesken, N.J.; Kleist, J. The Relationship of Drought Frequency and Duration to Time Scales. In Proceedings of the 8th Conference on Applied Climatology, Anaheim, CA, USA, 17–22 January 1993; Department of Atmospheric Science Colorado State University: Fort Collins, CO, USA, 1993; Volume 17, pp. 179–184.
28. Adams, J. Climate_Indices, an Open Source Python Library Providing Reference Implementations of Commonly Used Climate Indices. Available online: https://github.com/monocongo/climate_indices (accessed on 24 April 2023).
29. Zhang, Y.; Hao, Z.; Zhang, Y. Agricultural Risk Assessment of Compound Dry and Hot Events in China. *Agric. Water Manag.* **2023**, *277*, 108128. [CrossRef]
30. Li, W.; Jiang, Z.; Li, L.Z.X.; Luo, J.-J.; Zhai, P. Detection and Attribution of Changes in Summer Compound Hot and Dry Events over Northeastern China with CMIP6 Models. *J. Meteor. Res.* **2022**, *36*, 37–48. [CrossRef]
31. Wang, Q.; Wang, L.; Huang, G.; Piao, J.; Chotamonsak, C. Temporal and Spatial Variation of the Transitional Climate Zone in Summer during 1961–2018. *Int. J. Climatol.* **2021**, *41*, 1633–1648. [CrossRef]
32. Wang, L.; Chen, W.; Fu, Q.; Huang, G.; Wang, Q.; Chotamonsak, C.; Limsakul, A. Super Droughts over East Asia since 1960 under the Impacts of Global Warming and Decadal Variability. *Int. J. Climatol.* **2022**, *42*, 4508–4521. [CrossRef]
33. Lawrence, D.M.; Fisher, R.A.; Koven, C.D.; Oleson, K.W.; Swenson, S.C.; Bonan, G.; Collier, N.; Ghimire, B.; van Kampenhout, L.; Kennedy, D.; et al. The Community Land Model Version 5: Description of New Features, Benchmarking, and Impact of Forcing Uncertainty. *J. Adv. Model. Earth Syst.* **2019**, *11*, 4245–4287. [CrossRef]
34. Lawrence, D.; Fisher, R.; Koven, C.; Oleson, K.; Swenson, S.; Vertenstein, M. Technical Description of Version 5.0 of the Community Land Model (CLM). 2018. Available online: https://www.cesm.ucar.edu/models/clm/docs (accessed on 8 August 2022).
35. Cucchi, M.; Weedon, G.P.; Amici, A.; Bellouin, N.; Lange, S.; Müller Schmied, H.; Hersbach, H.; Buontempo, C. WFDE5: Bias-Adjusted ERA5 Reanalysis Data for Impact Studies. *Earth Syst. Sci. Data* **2020**, *12*, 2097–2120. [CrossRef]
36. Hilton, T.W.; Loik, M.E.; Campbell, J.E. Simulating International Drought Experiment Field Observations Using the Community Land Model. *Agric. For. Meteorol.* **2019**, *266–267*, 173–183. [CrossRef]
37. Joiner, J.; Yoshida, Y.; Zhang, Y.; Duveiller, G.; Jung, M.; Lyapustin, A.; Wang, Y.; Tucker, C.J. Estimation of Terrestrial Global Gross Primary Production (GPP) with Satellite Data-Driven Models and Eddy Covariance Flux Data. *Remote Sens.* **2018**, *10*, 1346. [CrossRef]
38. Martens, B.; Miralles, D.G.; Lievens, H.; Van Der Schalie, R.; De Jeu, R.A.M.; Fernández-Prieto, D.; Beck, H.E.; Dorigo, W.A.; Verhoest, N.E.C. GLEAM v3: Satellite-Based Land Evaporation and Root-Zone Soil Moisture. *Geosci. Model Dev.* **2017**, *10*, 1903–1925. [CrossRef]
39. Miralles, D.G.; Holmes, T.R.H.; De Jeu, R.A.M.; Gash, J.H.; Meesters, A.G.C.A.; Dolman, A.J. Global Land-Surface Evaporation Estimated from Satellite-Based Observations. *Hydrol. Earth Syst. Sci.* **2011**, *15*, 453–469. [CrossRef]
40. Martens, B.; Waegeman, W.; Dorigo, W.A.; Verhoest, N.E.C.; Miralles, D.G. Terrestrial Evaporation Response to Modes of Climate Variability. *NPJ Clim. Atmos. Sci.* **2018**, *1*, 43. [CrossRef]
41. Good, S.P.; Moore, G.W.; Miralles, D.G. A Mesic Maximum in Biological Water Use Demarcates Biome Sensitivity to Aridity Shifts. *Nat. Ecol. Evol.* **2017**, *1*, 1883–1888. [CrossRef] [PubMed]
42. Schumacher, D.L.; Keune, J.; Van Heerwaarden, C.C.; Vilà-Guerau De Arellano, J.; Teuling, A.J.; Miralles, D.G. Amplification of Mega-Heatwaves through Heat Torrents Fuelled by Upwind Drought. *Nat. Geosci.* **2019**, *12*, 712–717. [CrossRef]
43. Reichstein, M.; Bahn, M.; Ciais, P.; Frank, D.; Mahecha, M.D.; Seneviratne, S.I.; Zscheischler, J.; Beer, C.; Buchmann, N.; Frank, D.C.; et al. Climate Extremes and the Carbon Cycle. *Nature* **2013**, *500*, 287–295. [CrossRef]
44. Li, X.; Li, Y.; Chen, A.; Gao, M.; Slette, I.J.; Piao, S. The Impact of the 2009/2010 Drought on Vegetation Growth and Terrestrial Carbon Balance in Southwest China. *Agric. For. Meteorol.* **2019**, *269–270*, 239–248. [CrossRef]
45. Deng, Y.; Wang, X.; Wang, K.; Ciais, P.; Tang, S.; Jin, L.; Li, L.; Piao, S. Responses of Vegetation Greenness and Carbon Cycle to Extreme Droughts in China. *Agric. For. Meteorol.* **2021**, *298–299*, 108307. [CrossRef]
46. Teuling, A.J.; Seneviratne, S.I.; Stöckli, R.; Reichstein, M.; Moors, E.; Ciais, P.; Luyssaert, S.; Van Den Hurk, B.; Ammann, C.; Bernhofer, C.; et al. Contrasting Response of European Forest and Grassland Energy Exchange to Heatwaves. *Nat. Geosci.* **2010**, *3*, 722–727. [CrossRef]
47. Xu, H.; Wang, X.; Zhao, C.; Yang, X. Diverse Responses of Vegetation Growth to Meteorological Drought across Climate Zones and Land Biomes in Northern China from 1981 to 2014. *Agric. For. Meteorol.* **2018**, *262*, 1–13. [CrossRef]
48. Giardina, F.; Konings, A.G.; Kennedy, D.; Alemohammad, S.H.; Oliveira, R.S.; Uriarte, M.; Gentine, P. Tall Amazonian Forests Are Less Sensitive to Precipitation Variability. *Nat. Geosci.* **2018**, *11*, 405–409. [CrossRef]
49. Xu, W.; Yuan, W.; Wu, D.; Zhang, Y.; Shen, R.; Xia, X.; Ciais, P.; Liu, J. Impacts of Record-Breaking Compound Heatwave and Drought Events in 2022 China on Vegetation Growth. *Agric. For. Meteorol.* **2024**, *344*, 109799. [CrossRef]
50. Boeck, H.J.D.; Dreesen, F.E.; Janssens, I.A.; Nijs, I. Whole-system Responses of Experimental Plant Communities to Climate Extremes Imposed in Different Seasons. *New Phytol.* **2010**, *189*, 806–817. [CrossRef]

51. Xu, H.; Xiao, J.; Zhang, Z. Heatwave Effects on Gross Primary Production of Northern Mid-Latitude Ecosystems. *Environ. Res. Lett.* **2020**, *15*, 074027. [CrossRef]
52. Flach, M.; Sippel, S.; Gans, F.; Bastos, A.; Brenning, A.; Reichstein, M.; Mahecha, M.D. Contrasting Biosphere Responses to Hydrometeorological Extremes: Revisiting the 2010 Western Russian Heatwave. *Biogeosciences* **2018**, *15*, 6067–6085. [CrossRef]
53. Ristic, Z.; Momčilović, I.; Bukovnik, U.; Prasad, P.V.V.; Fu, J.; DeRidder, B.P.; Elthon, T.E.; Mladenov, N. Rubisco Activase and Wheat Productivity under Heat-Stress Conditions. *J. Exp. Bot.* **2009**, *60*, 4003–4014. [CrossRef]
54. Meinzer, F.C.; Johnson, D.M.; Lachenbruch, B.; McCulloh, K.A.; Woodruff, D.R. Xylem Hydraulic Safety Margins in Woody Plants: Coordination of Stomatal Control of Xylem Tension with Hydraulic Capacitance. *Funct. Ecol.* **2009**, *23*, 922–930. [CrossRef]
55. Zhang, W.; Luo, M.; Gao, S.; Chen, W.; Hari, V.; Khouakhi, A. Compound Hydrometeorological Extremes: Drivers, Mechanisms and Methods. *Front. Earth Sci.* **2021**, *9*, 673495. [CrossRef]
56. López, R.; Ramírez-Valiente, J.A.; Pita, P. How Plants Cope with Heatwaves in a Drier Environment. *Flora* **2022**, *295*, 152148. [CrossRef]
57. Rousi, E.; Kornhuber, K.; Beobide-Arsuaga, G.; Luo, F.; Coumou, D. Accelerated Western European Heatwave Trends Linked to More-Persistent Double Jets over Eurasia. *Nat. Commun.* **2022**, *13*, 3851. [CrossRef] [PubMed]
58. Seneviratne, S.I.; Lüthi, D.; Litschi, M.; Schär, C. Land–Atmosphere Coupling and Climate Change in Europe. *Nature* **2006**, *443*, 205–209. [CrossRef]